EMM EMUS Observations of Hot Oxygen Corona at Mars: Radial Distribution and Temporal Variability

Krishnaprasad Chirakkil[1,2], Justin Deighan[1], Michael S. Chaffin[1], Sonal K. Jain[1], Robert J. Lillis[3], Susarla Raghuram[1,2], Greg Holsclaw[1], David A. Brain[1], Ed Thiemann[1], Phil Chamberlin[1], Matthew O. Fillingim[3], Scott Evans[4], Scott England[5], Hessa AlMatroushi[6], Hoor AlMazmi[7], Frank Eparvier[1], Marko Gacesa[8], Nayla El-Kork[2,8], Shannon Curry[3]

[1]Laboratory for Atmospheric and Space Physics, University of Colorado Boulder, Boulder, CO, USA
[2]Space and Planetary Science Center, Khalifa University, Abu Dhabi, UAE
[3]Space Sciences Laboratory, University of California, Berkeley, CA, USA
[4]Computational Physics Inc., Springfield, VA, USA
[5]Department of Aerospace and Ocean Engineering, Virginia Polytechnic Institute and State University, Blacksburg, VA, USA
[6]Mohammed Bin Rashid Space Centre, Dubai, UAE
[7]United Arab Emirates Space Agency, Abu Dhabi, UAE
[8]Department of Physics, Khalifa University, Abu Dhabi, UAE

Key Points:

- Brighter O corona is observed during perihelion and dimmer during aphelion, indicating a strong relationship with the Sun–Mars distance
- The variation in OI 130.4 nm brightness shows a linear correlation with solar EUV irradiance, with a short–term solar rotation periodicity
- Interannual variability is observed from MY 36 to MY 37, showing an enhancement in O corona brightness with the rise of Solar Cycle 25

Corresponding author: Krishnaprasad Chirakkil, krishnaprasad.chirakkil@lasp.colorado.edu

Abstract

We present the first observations of the dayside coronal oxygen emission in far ultraviolet (FUV) measured by the Emirates Mars Ultraviolet Spectrometer (EMUS) onboard the Emirates Mars Mission (EMM). The high sensitivity of EMUS is providing an opportunity to observe the tenuous oxygen corona in FUV, which is otherwise difficult to observe. Oxygen resonance fluorescence emission at 130.4 nm provides a measurement of the upper atmospheric and exospheric oxygen. 471 oxygen corona profiles are constructed using the long–exposure time cross–exospheric mode (OS4) of EMUS observations. The profiles range from ∼200 km altitude up to several Mars radii (>6 R_M) across all seasons and for two Mars years. Our analysis shows that OI 130.4 nm is highly correlated with solar irradiance as well as changes in the Sun–Mars distance. The prominent short term periodicity in oxygen corona brightness is consistent with the solar rotation period (quasi–27–days). A comparison between the perihelion seasons of Mars Year (MY) 36 and MY 37 shows interannual variability with enhanced emission intensities during MY 37. These observations show a highly variable oxygen corona, which has significant implications on constraining the photochemical escape of atomic oxygen from Mars.

Plain Language Summary

Emirates Mars Ultraviolet Spectrometer (EMUS) onboard Emirates Mars Mission (EMM) is capable of observing ultraviolet emissions emanating from Mars. Oxygen in Martian exosphere is hard to see because it's tenuous. In this study, the analysis of the long exposure time EMUS observations show that the hot oxygen corona on Mars has a short term variability due to solar rotation. Hot oxygen corona also shows a long–term variability that depends on the Sun–Mars distance and the solar cycle progression. When comparing data from two Martian years, it is noticed that the oxygen corona became brighter when the Sun is more active.

1 Prior Studies of the Hot Oxygen Corona at Mars

Atomic oxygen in the Martian atmosphere is produced by the photodissociation of atmospheric carbon dioxide (Nier & McElroy, 1977; Barth et al., 1971). Atomic oxygen is the dominant neutral species in the Martian upper atmosphere, and quantifying its loss budget is important for understanding the evolution of CO_2 and H_2O reservoirs at Mars (Deighan et al., 2015). Oxygen in the collisional thermosphere is called thermal (or cold) oxygen, while that in the exosphere is called non-thermal (or hot) oxygen. Dissociative recombination of O_2^+ in the ionosphere is the primary source of hot oxygen atoms, and hence this reaction is an important loss mechanism for oxygen from Mars (McElroy, 1972; Lillis et al., 2017). Dissociative recombination of O_2^+ can take place via five channels (Fox & Haćić, 2009):

$$\begin{aligned} O_2^+ + e^- &\longrightarrow O(^3P) + O(^3P) \quad 7.0\ \text{eV} \\ &\longrightarrow O(^3P) + O(^1D) \quad 5.0\ \text{eV} \\ &\longrightarrow O(^3P) + O(^1S) \quad 2.8\ \text{eV} \\ &\longrightarrow O(^1D) + O(^1D) \quad 3.1\ \text{eV} \\ &\longrightarrow O(^1D) + O(^1S) \quad 0.8\ \text{eV} \end{aligned}$$

The mean excess energy released in the dissociative recombination channels is equally shared between the two newly formed oxygen atoms. The first two channels, which are highly exothermic, results in oxygen atoms having enough energy (more than the escape energy of ∼2 electron volts at exobase) to escape the gravitational pull of the planet. The output of the third channel has been found to be minimal, while the last two channels are dependent on the vibrational state of O_2^+. Other photochemical processes and sputtering

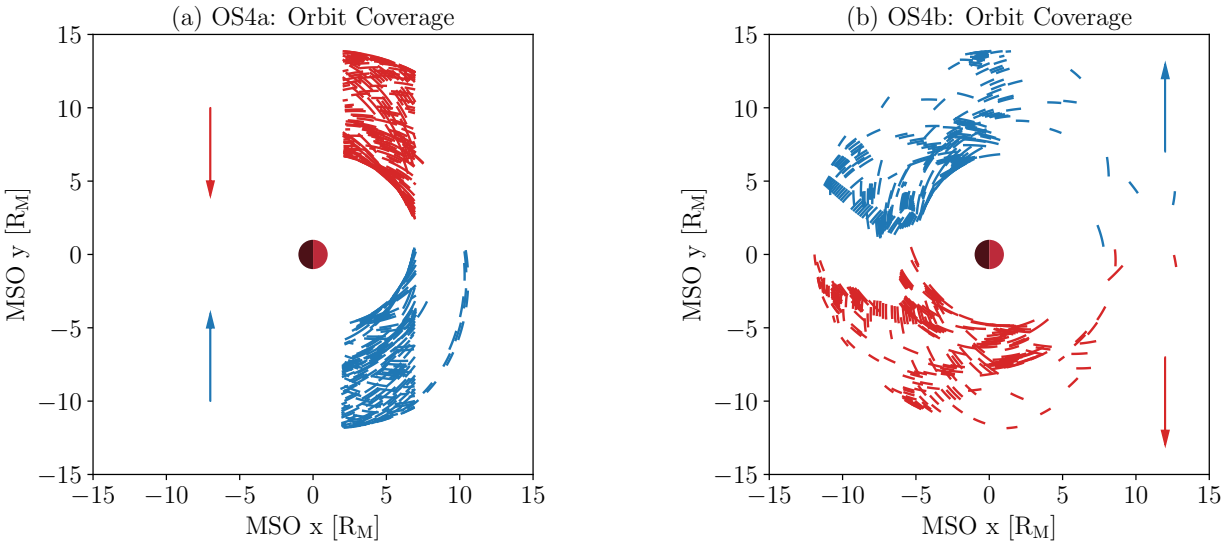

Figure 1. Location of EMM with pointing directions for a) EMUS OS4a foreground corona observations on the dayside b) EMUS OS4b interplanetary background observations. The arrows represent the look directions (towards Mars for OS4a and away from Mars for OS4b) with the red and blue arrows showing opposite look directions.

are thought to operate in the Martian atmosphere, but are less important in the current epoch (Gröller et al., 2014; Fox & Hać, 2018, 2014; Cravens et al., 2017).

The oxygen atoms that are unable to escape from Mars are bound to the atmosphere form a corona, which is an extended diffuse population of hot oxygen atoms that surrounds the planet for several planetary radii. These oxygen atoms are either produced from the less energetic dissociative recombination channels or through collisions with other atoms and molecules. However, observing the oxygen corona has proven to be difficult due to its tenuous nature (Deighan et al., 2015; Carveth et al., 2012). Previous studies have attempted to observe it by using remote sensing measurements that focus on the relatively strong OI 130.4 nm triplet. Solar resonant scattering is the main source for the OI 130.4 nm emission line on Mars, which consists of three resonance triplet transitions of atomic oxygen at 130.2, 130.5, and 130.6 nm respectively (Strickland et al., 1972, 1973). SPICAM/Mars Express observed the oxygen corona below ∼500 km (Montmessin et al., 2017) and ALICE/Rosetta observed the oxygen corona below ∼1300 km during its flyby maneuver with a limited altitude sampling (Feldman et al., 2011). Despite this, the expected brightness at altitudes above 700 km, where the hot oxygen population dominates, is only between 1 to 10 Rayleighs, and had been very difficult to observe (Deighan et al., 2015).

The Martian atomic oxygen exosphere is observed to have two components (Deighan et al., 2015), as predicted by McElroy and Donahue (1972). This dual population of the exosphere is seen when looking at the variation in altitude of the brightness of the 130.4 nm atomic oxygen resonant emission. This variation displays a clear two-slope altitude dependence, with a rapid decrease in brightness just above the exobase, followed by a much slower decrease from typically 600 km altitude above the surface of Mars (Deighan et al., 2015) (also see Figure 4a). The less energetic component in the lower altitudes with a small-scale height is attributed to the thermal expansion of Mars' atomic oxygen component above the Martian exobase, which is the thermal component of the oxygen exosphere (Chaufray et al., 2015; Jain et al., 2015). The more energetic component above 600 km is thought to be produced primarily by two processes occurring in Mars' upper

atmosphere. These are the dissociative recombination of the most abundant ion, O_2^+, in Mars' ionosphere as mentioned above (Lee, Combi, Tenishev, Bougher, Deighan, et al., 2015; Lee, Combi, Tenishev, Bougher, & Lillis, 2015) and the sputtering of the upper atmosphere by precipitating pickup ions (Leblanc et al., 2015). These processes are thought to be the two main channels of Mars' neutral atmospheric oxygen escape (Chaufray et al., 2007, 2009; Yagi et al., 2012).

An indirect signature of Mars' neutral oxygen escape was observed for the first time by ALICE instrument on board Rosetta (Feldman et al., 2011) and was confirmed by the Imaging Ultraviolet Spectrograph (IUVS) instrument on board Mars Atmosphere and Volatile Evolution (MAVEN) spacecraft. Energetic oxygen pickup ions observed by SEP (Solar Energetic Particle), SWIA (Solar Wind Ion Analyzer), and STATIC (Supra-Thermal and Thermal Ion Composition) instruments on board MAVEN were used to infer exospheric oxygen densities and oxygen escape rates (Rahmati et al., 2017, 2015, 2018).

In this study, we use 471 coronal emission profiles from ∼25 months (∼1.11 Mars years consisting of observations from Mars Year 36 and early Mars Year 37) of Emirates Mars Mission (EMM)/Emirates Mars Ultraviolet Spectrometer (EMUS) data to understand and characterize the variability in the OI 130.4 nm coronal emission with the Martian seasons and solar forcing conditions. The following sections describe the instruments and data used, the observations and discussion. Finally, the paper concludes by summarizing the observations and describing the prospects for future work.

2 EMUS Cross Exospheric and Background Observations

In February 2021, the EMM spacecraft entered orbit around Mars and began to study the atmosphere of Mars (Amiri et al., 2022; Almatroushi et al., 2021). EMM has a ∼55 hour period science orbit with a ∼20,000 km periapsis and ∼43,000 km apoapsis (6.9 R_M × 13.7 R_M), and an orbital inclination of 25°. This unique orbit provides near-complete geographic and diurnal coverage of Mars every ∼10 days (Amiri et al., 2022). EMM carries the EMUS instrument (Holsclaw et al., 2021), which is an EUV/FUV spectrometer sensitive to wavelengths between ∼100 nm and 170 nm. Light enters the spectrometer through a narrow 0.6° × 11° slit. It is then focused by a spherical mirror onto a diffraction grating. The grating splits the light into different "colors" (i.e. its spectral components). This results in a two-dimensional image on a microchannel plate (MCP) detector with spectral and spatial dimensions. Photon counts in each spatial and spectral bin is recorded in 50 second integrations for corona observations, called OS4 mode. Holsclaw et al. (2021) describes in detail the EMUS instrument, its science goals and the different observation strategies.

EMUS OS4 mode is designed to make coronal observations with a high signal to noise ratio. This observation provides long exposure times for the inner, middle and outer Martian exosphere. This mode is designed to occur when the spacecraft is charging in a near-inertial orientation (Holsclaw et al., 2021). There are two scenarios for this observation strategy: exospheric or coronal observations (OS4a) and interplanetary background observations (OS4b). OS4a is a cross-exosphere observation mode (or a limb scan that is made farther away from the planet's bright limb) by pointing the instrument across the EMM orbit and along the Sun–Mars line. The instrument boresight vector is pointed in the plane of the spacecraft orbit, perpendicular to both the Mars–Sun line and the orbit normal. EMUS is observing lines of sight for tangent altitudes from 200 km to >17,000 km (1.06 R_M to >6 R_M) such that the boresight intersects the Mars–centered Solar Orbital (MSO) X-Z plane (Holsclaw et al., 2021). The spectral resolution (or instrument slit position) is 1.8 nm, which ensures adequate signal to noise while still spectrally separating the 130.4 nm oxygen signal from neighboring lines. OS4b targets the interplanetary background and points in the same direction (within 2°) of the OS4a that occurred on the opposite side of the orbit, such that the EMUS boresight does not intersect the MSO X-Z plane. The purpose of OS4b measure-

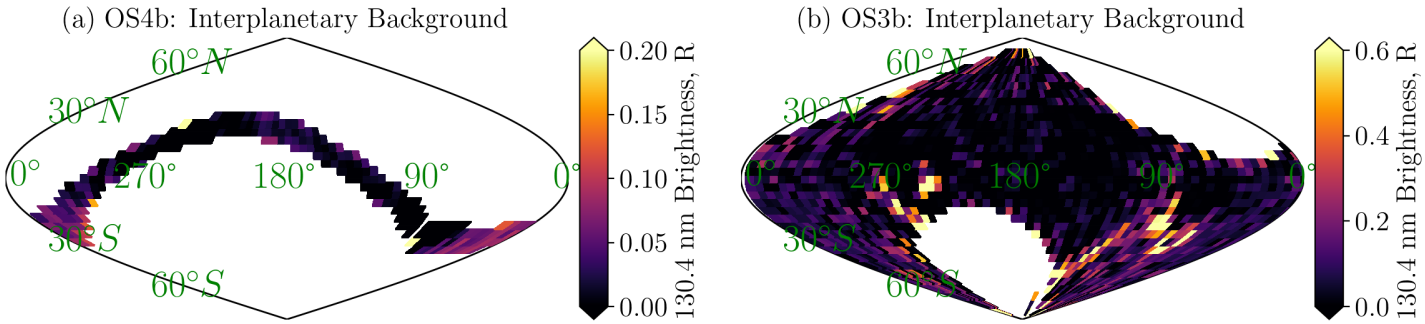

Figure 2. Sky maps of interplanetary background at 130.4 nm in ecliptic J2000 coordinates using a) EMUS OS4b background observations and b) EMUS OS3b background observations. The observations are binned in 5 degree ecliptic longitude by 5 degree ecliptic latitude bins. The bright patches correspond to the periods when the galactic plane was in the instrument viewing direction.

ment is to distinguish the coronal foreground emission from the interplanetary background emissions (Holsclaw et al., 2021).

The major backgrounds to the oxygen 130.4 nm emission is the 1) hydrogen Lyman alpha wing background and the 2) interplanetary background. Hydrogen Lyman alpha (HI 121.6 nm) is by far the brightest emission line in EMUS data, and all other emissions are sitting either on the shorter wavelength side or the longer wavelength side of this bright emission feature, called the Line Spread Function (LSF). This background is subtracted by calculating the baseline fit based on the shorter wavelength and longer wavelength sides of 130.4 nm core, that falls on the Lyman alpha wing, but not on the 130.4 nm emission feature itself. More details of H Lyman alpha wing subtraction from OI 130.4 nm emission is provided in the Supporting Information (see Figure S4 of SI).

The interplanetary background is due to emissions originating from the sky that are unrelated to the oxygen corona, but are emitted by the interplanetary sources such as dust, interstellar medium, and diffuse emissions from the galactic plane. This background is subtracted by using the OS4b mode of observations, which is designed to observe the interplanetary background corresponding to each of the coronal (OS4a) observations. We find the nearest available background observation (OS4b) corresponding to each of the foreground coronal observation (OS4a) to perform the subtraction. In addition to these two prominent backgrounds, continuum emissions due to bright stars are also common. These appear as bright features that contaminate certain pixels of the image. A star subtraction algorithm has been developed to remove this stellar contamination. This method works by identifying and removing the contaminated pixels by looking at the higher wavelength (132.5 nm to 162 nm, avoiding both OI 130.4 nm and the HI 121.6 nm ghost feature near 163 nm at the nominal grating position) where we don't expect any emissions from the Mars exosphere, while the stars are still featured.

3 Altitude, Solar Zenith Angle and Seasonal Variability

Figures 1a and 1b shows the orbit coverage in the Mars–centered Solar Orbital (MSO) coordinate system. MSO +X is sunward from the center of the planet, +Y is duskward, and the Z direction completes the right–handed system with +Z towards the north ecliptic pole. Figure 1a shows the segments of orbits where cross-exospheric observations (OS4a) were made on the dayside, while Figure 1b shows the segments of orbits where interplanetary background observations (OS4b) were made by looking away from Mars. Additional

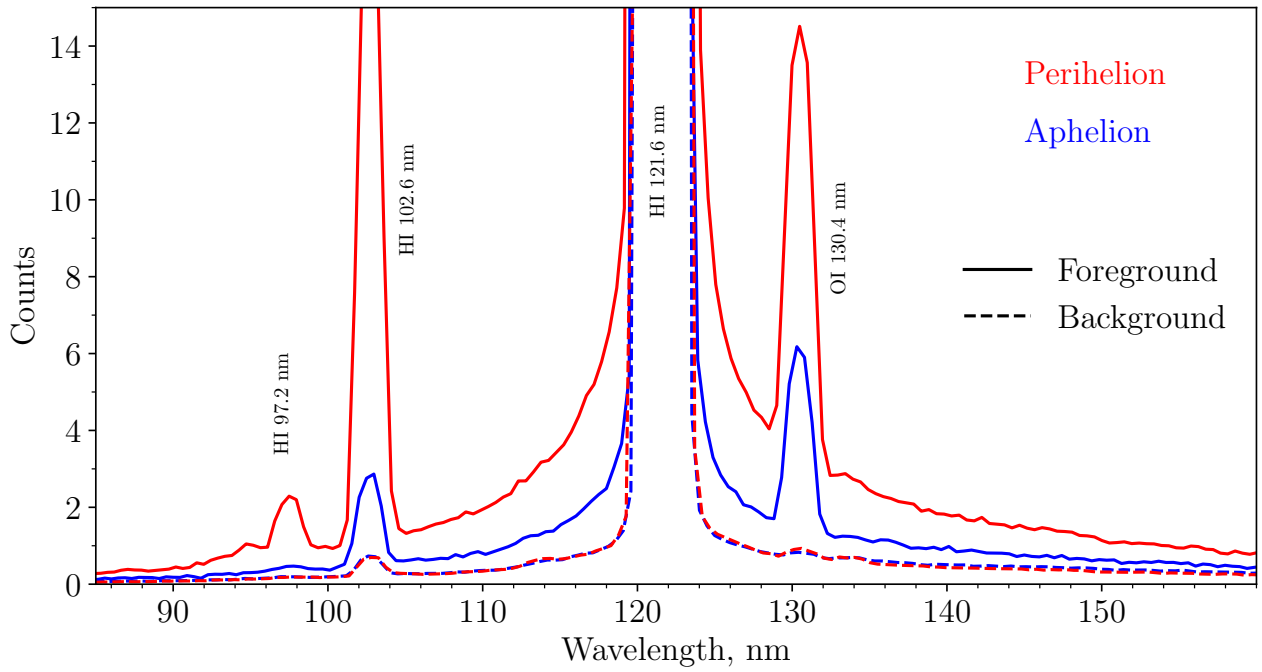

Figure 3. Examples of coronal (solid curve) and interplanetary background (dashed curve) spectra observed by EMUS for aphelion and perihelion seasons. The tangent altitude range co-added for obtaining the foreground spectra is 2000 to 2500 km. The corresponding integration time for the foreground spectra is ∼9 minutes. The integration time for the background spectra is ∼57 minutes. For the examples shown above, the aphelion corona spectra is obtained on August 12, 2021, while the corresponding background spectra is obtained on August 11, 2021. The perihelion corona spectra is obtained on June 5, 2022, while the corresponding background spectra is obtained on June 8, 2022.

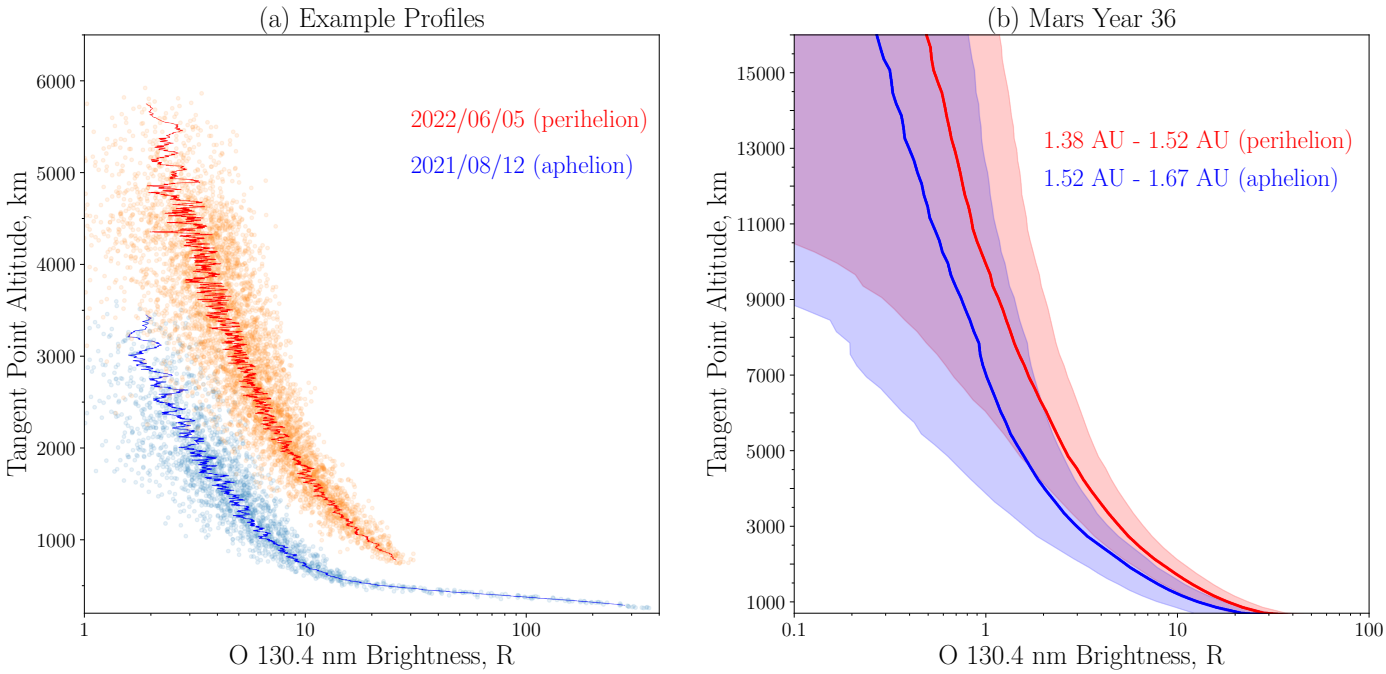

Figure 4. a) Example brightness vs. altitude profiles obtained using the same set of observations as in Figure 3 for aphelion (August 12, 2021) and perihelion (June 5, 2022) periods. The scattered points are individual samples (pixels) and the solid lines are the 20-samples rolling averages, b) averaged brightness vs. altitude profiles with 1σ errorbars for MY 36 shown for two ranges of Sun–Mars distance, viz. perihelion (1.38–1.52 AU) and aphelion (1.52–1.67 AU) in red and blue respectively.

information on geographic coverage, sky coverage, coverage of tangent altitudes, solar zenith angle, Sun–Mars distance, right ascension and declination are provided in the Supporting Information (see Figures S1, S2, and S3 of SI).

Figure 2 shows the maps of interplanetary background at 130.4 nm wavelength. Figure 2a is made with the OS4b mode of observations, while Figure 2b is made with an observation mode of EMUS called OS3b. OS3b has more coverage on the sky, but are quick scans (integration time of 0.7 seconds) designed mainly for hydrogen Lyman alpha observations (Holsclaw et al., 2021). These background observations, especially OS4b, allows for the oxygen from the Martian exosphere to be distinguished from the interplanetary emission contributions. The images show the presence of two bright regions on the sky, mainly due to the presence of galactic plane in the line of sight during those observation periods.

Figure 3 shows the examples of EMUS OS4 spectra during aphelion period (that is, when Mars and Sun were at the farthest) and perihelion period (that is, when Mars and Sun were at the closest). The solid curves show the coronal spectra (OS4a), while dashed curves show the interplanetary background spectra (OS4b). The aphelion corona spectra shown is obtained on August 12, 2021, while the corresponding background spectra is obtained on August 11, 2021. The perihelion corona spectra shown is obtained on June 5, 2022, while the corresponding background spectra is obtained on June 8, 2022. The perihelion spectra have generally higher intensities as compared to the aphelion spectra as expected. A tangent altitude range of 2000 to 2500 km is co-added for obtaining the foreground spectra. The corresponding integration time for the foreground spectra is ∼9 minutes. The integration time for the background spectra is ∼57 minutes. It may be noted that the background spectra during both periods are nearly of the same intensities. The difference in brightness enhancement for OI 130.4 nm and HI 102.6 nm emissions between the two seasons indicates their different emission sources.

Figure 4a shows the examples of OI 130.4 nm brightness vs. altitude profiles obtained using the same set of observations after background subtractions (both H Lyman alpha wing background and the interplanetary background). These observations are representative of several observations done using a similar strategy. The example days chosen for aphelion and perihelion are the same as in the spectra figure (Figure 3). Figure 4b shows the average brightness vs. altitude profiles for two ranges of Sun-Mars distance (1.38–1.52 AU and 1.52–1.67 AU). The errorbar (one standard deviation of the population) is shown as the color fill around the solid curves. Both Figures 4a and 4b clearly depict the brightness variation that is due to changing altitude as well as the changing Sun–Mars distance. It can be noted that higher brightness is observed during perihelion as compared to the aphelion.

Figure 5 shows the binned images of OI 130.4 nm brightness variation with altitude and as a function of Solar Zenith Angle (SZA) and Martian season (L_s). Figure 5a shows the variation of brightness as a function of altitude and SZA. Altitude and SZA are those of the tangent point of the line of sight. The altitude bin size is 500 km and the SZA bin size is 5 degree. The SZA variation during this period is 0 to ∼60 degree, making them on the dayside close to noon. Higher brightness is observed near noon as compared to higher SZAs. Figure 5b shows the brightness variation as a function of altitude and Martian season (L_s). Here also the altitude bin size is 500 km, and the L_s bin size is 10 degree. The contours of 0.5 R and 1.0 R are also shown for reference on both images. Figure 5c shows the timeline of brightness variation at four different altitude ranges from 1000 to 3000 km, each averaged over a 500 km altitude bin size. It can be seen that the oxygen corona is brighter during the perihelion season as compared to aphelion season at all the tangent altitudes shown here. Also, the interannual variability from MY 36 to MY 37 aphelion periods can be noted. The aphelion of MY 37 is brighter as compared to the aphelion of MY 36, primarily due to the rising Solar Cycle 25.

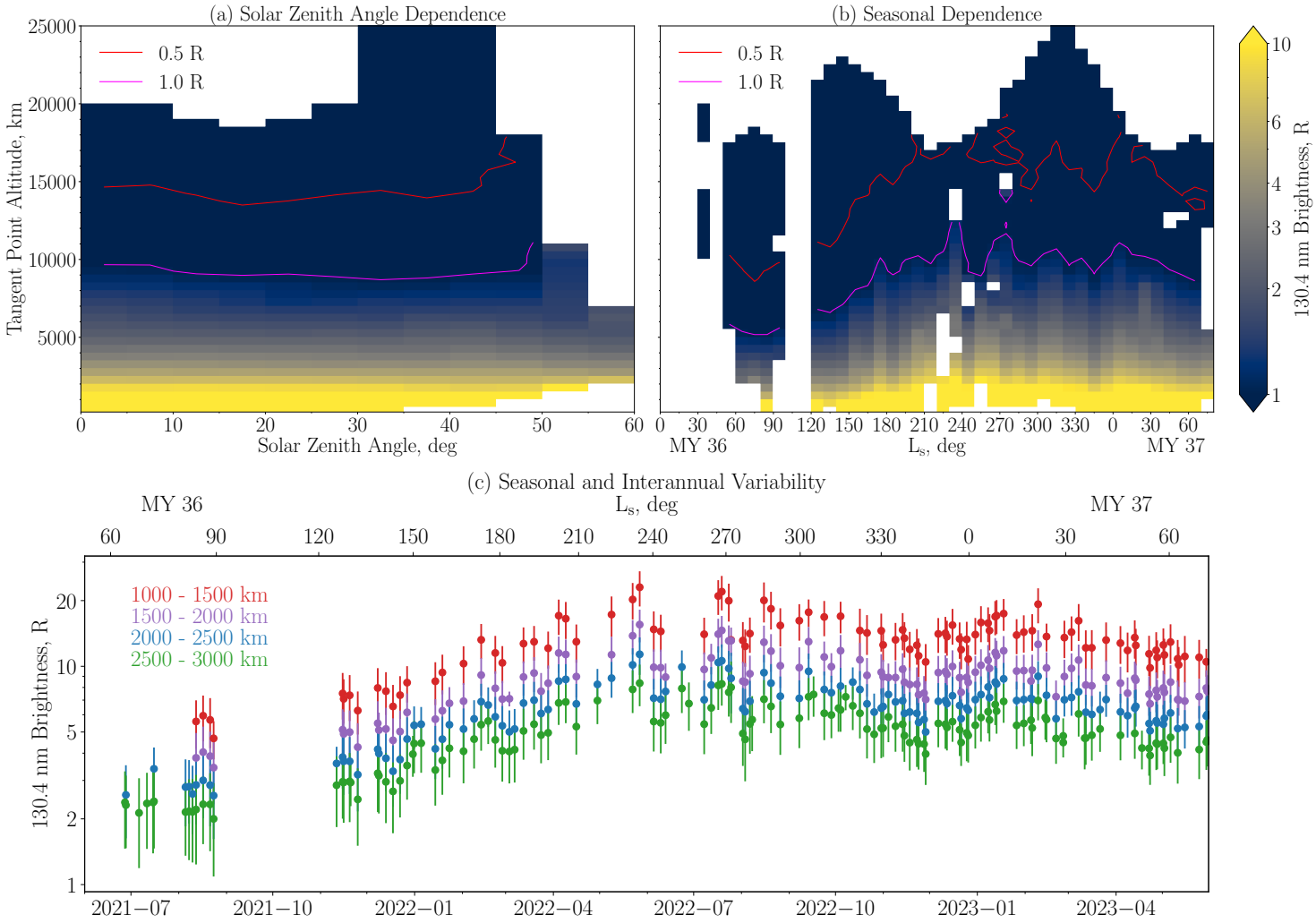

Figure 5. Binned images of OI 130.4 nm brightness as a function of a) Solar Zenith Angle (SZA) and altitude and b) Martian Solar Longitude (L_s) and altitude. The 0.5 R (red) and 1.0 R (magenta) contours are also shown. Panel c) shows the timeline of O corona brightness for four different altitude ranges from 1000 to 3000 km. Aphelion is when L_s is 71 deg. and perihelion is when L_s is 251 deg. Note that the brightness scale is logarithmic. Interannual variability during the aphelion periods of MY 36 and MY 37 can also be noted in Figures 5b and 5c. The data gap between L_s 100 and 120 in MY 36 is due to the absence of data collection during solar conjunction period.

4 Coronal Correlation with Solar Irradiance

Figure 6 shows the temporal variability of O corona brightness, solar irradiance and the backgrounds to coronal OI 130.4 nm emission. Figure 6a shows the EMUS observed 130.4 nm emission brightness at a tangent point altitude of 2000 km to 2500 km. The average and one standard deviation of the population as error bar is also shown. The range of values observed is shown as the scatter points. Figure 6b shows the temporal variability of solar 0–91 nm ionizing EUV irradiance and solar 130.4 nm irradiance from MAVEN/EUVM (Eparvier et al., 2015). EUVM has three calibrated photometers designed to measure the variability of the solar soft x-rays and EUV irradiance at Mars in three bands. In this study, we use the EUVM Level 3 modeled data, which is a combination of observations at Mars and time-interpolated observations at Earth using the spectral irradiance variability model called the Flare Irradiance Spectral Model-Mars (FISM-M) (Thiemann et al., 2017). The gap in the data from February 23, 2022 to April 21, 2022 is due to the absence of MAVEN/EUVM data during that period. Figure 6c shows the variation of hydrogen Lyman alpha wing under OI 130.4 nm. This background is subtracted from the original spectra to get the oxygen brightness values. Figure 6d shows the interplanetary background at 130.4 nm using the OS4b mode of observations. An error bar of one standard deviation of the population is also shown. The interplanetary (sky) background at 130.4 nm roughly varies around $\sim$ 0.1 R.

Figure 7 shows the same parameters normalized for Sun–Mars distance. The normalization is done to differentiate the variability in exospheric emission intensities and solar irradiance measured at Mars that varies with both Sun–Mars distance and solar activity progression. Figure 7a shows the O corona brightness normalized by $[1/r^4]$, where r is the Sun–Mars distance. The normalization by $[1/r^4]$ is done to account both the variation in ionizing radiation (which affects the production of hot O atoms), as well as the variation in fluorescence scattering (i.e., illumination conditions) with the changing Sun–Mars distance, with both factors contributing $[1/r^2]$ each. Figure 7b shows the solar irradiance normalized by a factor $[1/r^2]$. This is done to account the variation in solar irradiance measured at Mars with changing Sun–Mars distance. Figure 7c shows the H Lyman alpha wing under OI 130.4 nm normalized by $[1/r^2]$. Interestingly, we can notice that the seasonal variation in hydrogen intensities is still present in the normalized figure, with the peak intensity during southern summer solstice (L_s $\sim$270 degree). However, the O corona intensity peaks around the perihelion (L_s $\sim$251 degree). The increase in oxygen signal that is normalized by $[1/r^4]$ must be due to some combination of higher solar activity (which is clear), but also possibly in the source of hot O atoms, either due to electron temperatures (which mediate the rate of dissociative recombination), ion temperatures (which affect the distribution of initial hot O atom energies following the recombination reaction), or neutral density profiles (since collision with those neutrals affect the energy distribution of exospheric O atoms).

Figures 8a and 8b show the correlation between coronal 130.4 nm brightness and solar irradiances. Linear regression is used to fit the data points. Figure 8a shows the variation of coronal OI 130.4 nm as a function of solar ionizing irradiance (0–91 nm). Figure 8b shows the variation of coronal 130.4 nm as a function of solar 130.4 nm irradiance. Both plots indicate that the coronal oxygen brightness has a near linear relationship with the solar irradiance. Figure 8c is the correlation between coronal oxygen brightness and the product of solar ionizing irradiance and solar 130.4 nm emissions. The data points are having the highest goodness of fit and correlation coefficient with the product as compared to the individual irradiances. Coronal oxygen brightness is expected to vary positively with both solar EUV as well as the solar oxygen emission at 1304. nm. The first because EUV produces the ions necessary for dissociative recombination and the second because solar 130.4 nm is the source of illumination for the oxygen resonance line scattering in the corona that EMUS observes. The current analysis suggests that variations in the brightness of the hot coronal oxygen population at Mars are more strongly related with changes in ionizing solar EUV flux than the illuminating solar 130.4 nm line. The higher correlation of coronal

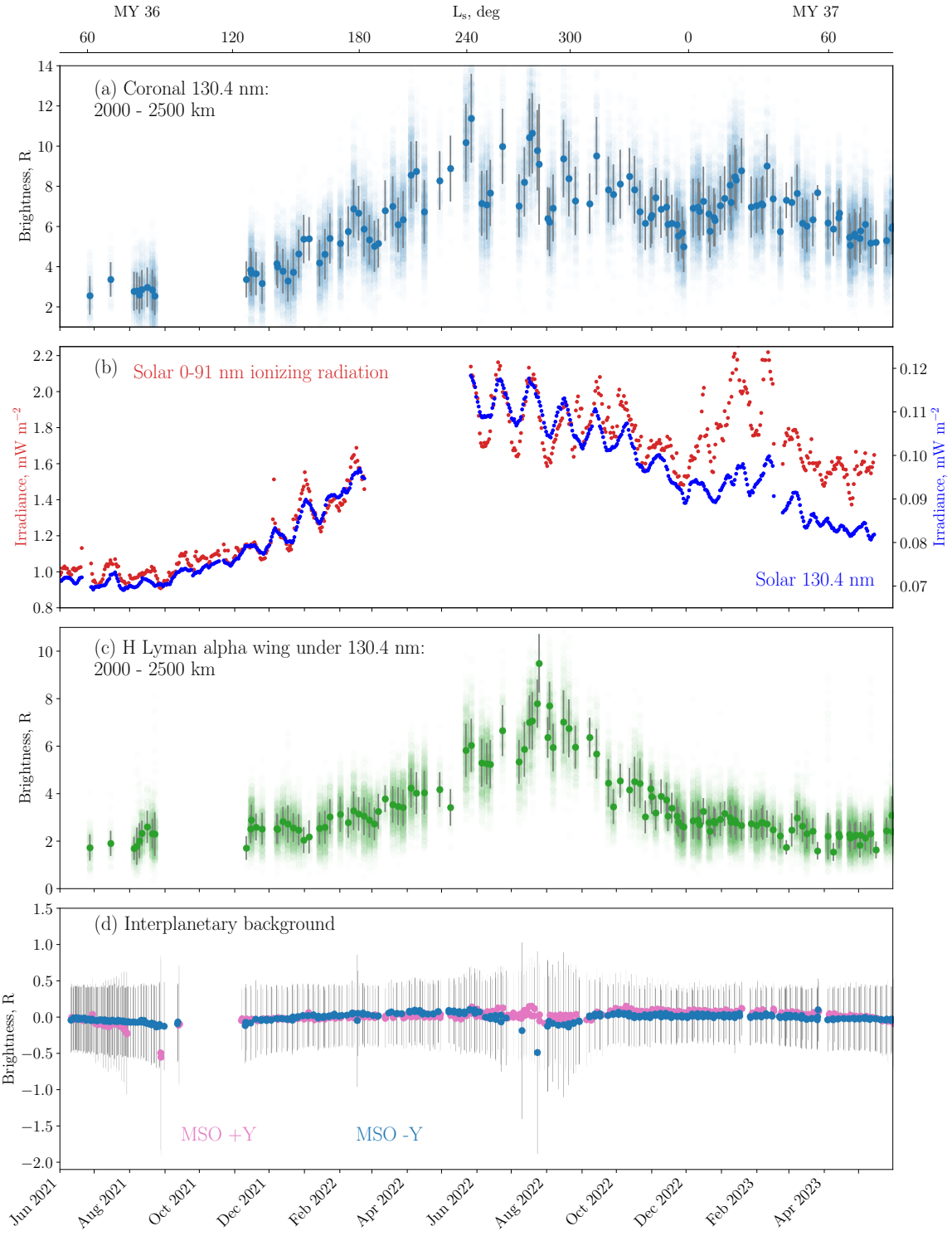

Figure 6. Temporal variability of a) OI 130.4 nm coronal brightness for an altitude range of 2000 to 2500 km, b) solar EUV 0-91 nm ionizing irradiance and solar 130.4 nm emissions at Mars, c) hydrogen Lyman alpha wing under EMUS OI 130.4 nm for the altitude range of 2000 to 2500 km, and d) interplanetary background at 130.4 nm, with 1σ errorbars. The gap in EMUS data between L_s 99 and 123 in MY 36 is due to the absence of EMM data collection during solar conjunction period. The gap in EUVM data between L_s 179 and 212 in MY 36 is due to the absence of MAVEN data collection during that period.

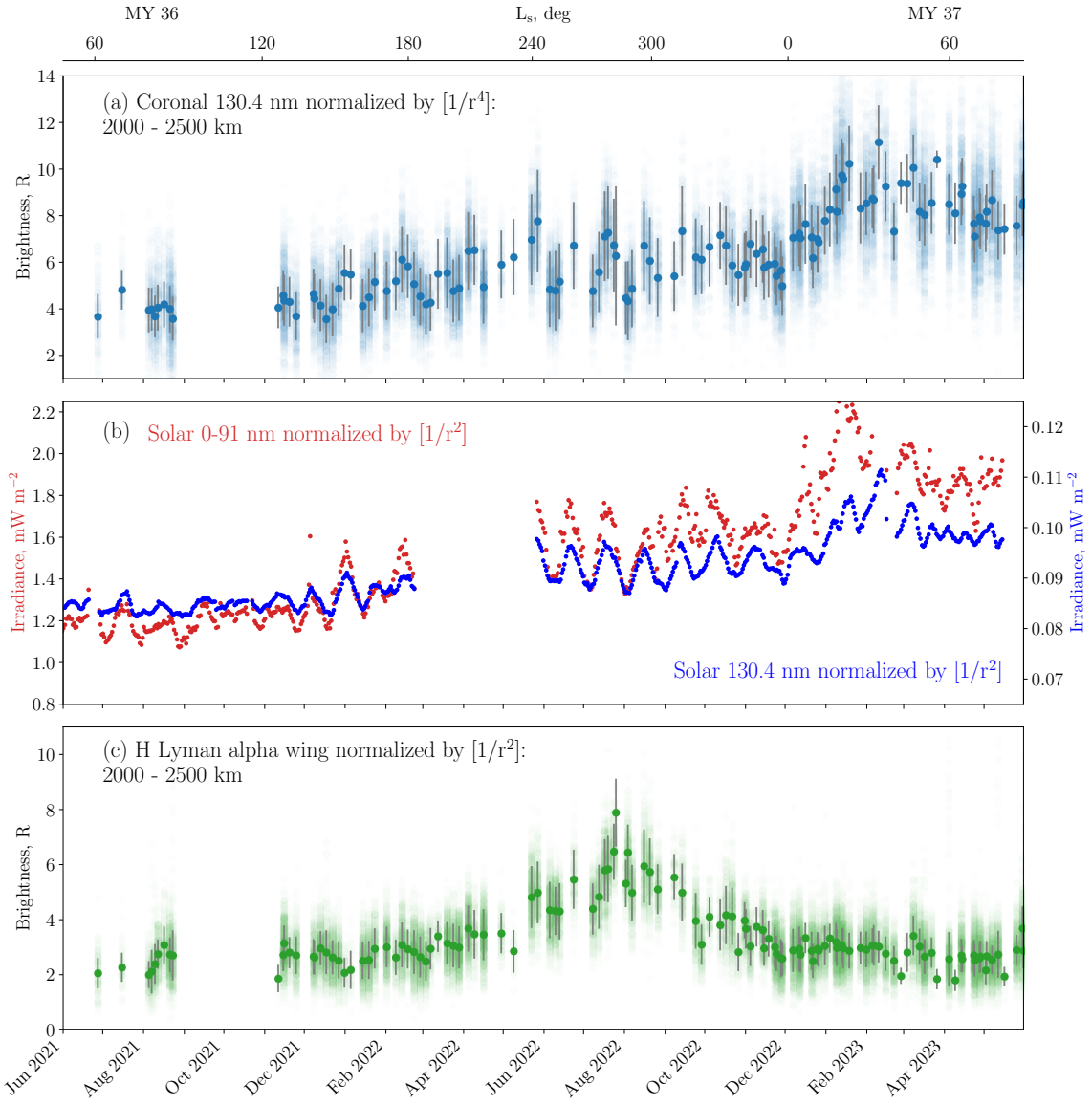

Figure 7. Temporal variability of coronal brightness and solar irradiance after normalizing for Sun–Mars distance. a) OI 130.4 nm coronal brightness normalized by $1/r^4$, where r is the Sun–Mars distance, b) solar irradiances at Mars normalized by $1/r^2$, and c) hydrogen Lyman alpha wing under OI 130.4 nm normalized by $1/r^2$. The gap in EMUS data between L_s 99 and 123 in MY 36 is due to the absence of EMM data collection during solar conjunction period. The gap in EUVM data between L_s 179 and 212 in MY 36 is due to the absence of MAVEN data collection during that period.

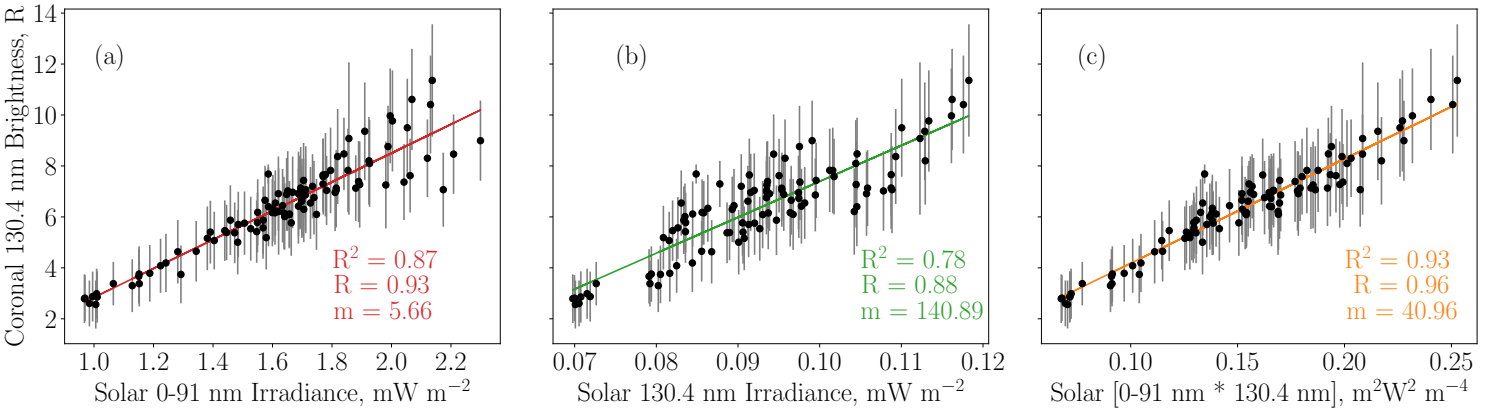

Figure 8. a) Correlation between solar EUV 0–91 nm ionizing irradiance and coronal oxygen 130.4 nm brightness, b) correlation between solar 130.4 nm and coronal oxygen 130.4 nm, and c) correlation between the product of solar EUV ionizing and solar 130.4 nm irradiances, and coronal oxygen 130.4 nm brightness. The coronal brightness is for an altitude range of 2000 – 2500 km. The symbol m is the slope of the fit with a unit of $R/mW/m^2$ for panels a and b, and with a unit of $R/m^2W^2/m^4$ for panel c. R is the correlation coefficient and R^2 is the goodness of fit.

brightness with EUV flux is consistent with an expected ionospheric photochemical source (Deighan et al., 2015). It may also be noted that photoelectron impact excitation source of OI 130.4 nm in the corona is negligible (Chaufray et al., 2015, 2009). Additionally, since this emission is optically thick, the scale height of the brightness is influenced by both density and temperature (Chaufray et al., 2015). Therefore, an increase in coronal brightness could imply an increase in coronal density.

4.1 Solar Rotation Effect in the Corona

The left side panels in Figure 9 show the time series of MAVEN EUVM data and EMM EMUS data normalized for Sun–Mars distance. The EMUS data shown is for a tangent altitude range of 2500 to 3000 km. The 81-days rolling average of the signal as well as the residual after subtracting the rolling average is also shown. The right side panels of Figure 9 show the Lomb-Scargle periodograms obtained using the residual EUVM and EMUS signals. The moving average is subtracted in order to remove the long term periodicities and their sub–harmonics in the data, which is caused by Sun–Mars distance variation, seasonal and annual variations.

The prominent short term periodicity in both the datasets is quasi–27–days due to solar rotation. The peak corresponding to solar rotation is above the 95% confidence level. Other prominent periodicities adjacent to the quasi–27–days are a result of the active regions contributing to the solar rotation variability being located at different latitudes. Also, solar rotation is differential with the equator rotating faster (taking only about 24 days) than the poles (which rotate once in more than 30 days) (Javaraiah, 2011). The periodograms for three other example altitude ranges (1000–1500 km in gray, 1500–2000 km in light purple, 2000–2500 km in light blue) are also shown in Figure 9d for comparison. We can notice that the Lomb-Scargle power for the main periodicity peak around quasi–27–days diminishes with increasing altitude (higher power for the combined range of 1000 to 2000 km as compared to the combined range of 2000 to 3000 km). This suggests that the effect of solar rotation is more pronounced in the lower corona as compared to the upper corona.

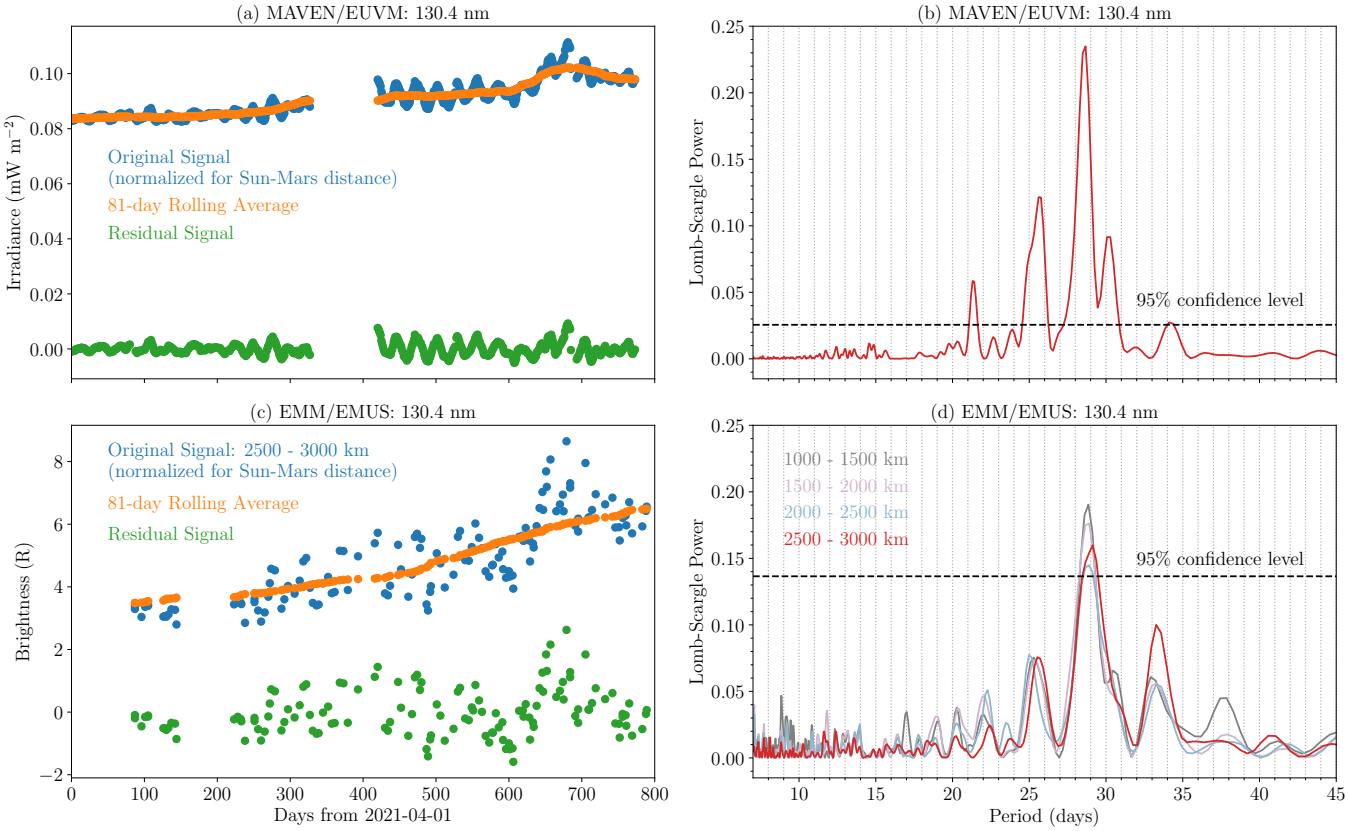

Figure 9. a) Time series of normalized EUVM 0-91 nm ionizing solar irradiance (blue), moving average corresponding to three solar rotations (orange), and the residual signal after subtracting the moving average (green). b) Lomb-Scargle periodogram for the residual EUVM signal (red). c) Time series of normalized EMUS OI 130.4 nm daily averaged coronal brightness for an altitude range of 2500 to 3000 km (blue), moving average corresponding to three solar rotations (orange), and the residual signal after subtracting the moving average (green). d) Lomb-Scargle periodogram for the residual EMUS signal (red). The 95% confidence level for both periodograms are also shown (black dashed lines). The other periodograms in the panel (d) are for three other altitude ranges in Figure 5c and are shown for comparison (1000–1500 km in gray, 1500–2000 km in light purple, 2000–2500 km in light blue).

5 Conclusions and Future Prospects

EMM/EMUS oxygen corona observations using the long exposure time scans reveal for the first time the dependence of brightness on Sun–Mars distance and solar forcing. EMUS OS4 data is highly sensitive to the OI 130.4 nm emission from the Martian exosphere and we have shown O corona observations upto an altitude of >6 R_M. The background observations enable us to subtract the interplanetary contributions to the foreground data. In addition to the strong Sun–Mars distance, solar zenith angle and solar EUV flux dependence, the O corona also shows a short term variability due to solar rotation. The prominent short term periodicity in both EUVM and EMUS data is the quasi–27–days solar rotation period. Correlation of the oxygen corona brightness with EUVM solar irradiance measurements suggests a relationship between coronal density and solar photoionizing flux. This supports the expectation that dissociative recombination in the ionosphere is the main source of hot oxygen on Mars.

The effects of episodic events such as solar flares and dust storms need to be investigated. The effect of crustal magnetic fields on the oxygen corona, if any, is also in need of investigation, although we do not expect to see any crustal field effects at these very high altitudes. The brightness observation is the first step to the derivation of exospheric density and temperature (Chaufray et al., 2009). The next step would be to calculate, using modeling, the escape rate of oxygen atoms that are escaping via non–thermal photochemical mechanisms. Escape flux of hot oxygen during different seasons can be calculated using these EMUS derived input parameters as well as the near–simultaneous in-situ neutral, ion and electron measurements from MAVEN (Lillis et al., 2017; Chirakkil et al., 2022; Cravens et al., 2017).

Open Research Section

Data Availability Statement

The EMM/EMUS l2a data we analyze here are available at the EMM Science Data Center (SDC, `https://sdc.emiratesmarsmission.ae/`). This location is designated as the primary repository for all data products produced by the EMM team and is designated as long–term repository as required by the UAE Space Agency. The data available (`https://sdc.emiratesmarsmission.ae/data`) include ancillary spacecraft data, instrument telemetry, Level 1 (raw instrument data) to Level 3 (derived science products), quicklook products, and data users guides (`https://sdc.emiratesmarsmission.ae/documentation`) to assist in the analysis of the data. Following the creation of a free login, all EMM data are searchable via parameters such as product file name, solar longitude, acquisition time, sub-spacecraft latitude and longitude, instrument, data product level, etc. EMUS data and users guides are available at: `https://sdc.emiratesmarsmission.ae/data/emus`. The MAVEN EUVM L3 data are publicly available at the NASA Planetary Data System through `https://pds-ppi.igpp.ucla.edu/data/maven-euv-modelled`.

Acknowledgments

Funding for development of the EMM mission is provided by the UAE government, and to co-authors outside of the UAE by MBRSC. KC and SR are supported by the grant 8474000332-KU-CU-LASP Space Sci. ET, PC, FE, and SC are supported by NASA through the MAVEN project.

References

Almatroushi, H., AlMazmi, H., AlMheiri, N., AlShamsi, M., AlTunaiji, E., Badri, K., ... Young, R. M. B. (2021, December). Emirates Mars Mission Characterization of Mars Atmosphere Dynamics and Processes. *Space Science Reviews*, *217*(8), 89. doi:

10.1007/s11214-021-00851-6

Amiri, H. E. S., Brain, D., Sharaf, O., Withnell, P., McGrath, M., Alloghani, M., ... Yousuf, M. (2022, February). The Emirates Mars Mission. *Space Science Reviews*, *218*(1), 4. doi: 10.1007/s11214-021-00868-x

Barth, C. A., Hord, C. W., Pearce, J. B., Kelly, K. K., Anderson, G. P., & Stewart, A. I. (1971). Mariner 6 and 7 ultraviolet spectrometer experiment: Upper atmosphere data. *Journal of Geophysical Research (1896-1977)*, *76*(10), 2213-2227. Retrieved from https://agupubs.onlinelibrary.wiley.com/doi/abs/10.1029/JA076i010p02213 doi: https://doi.org/10.1029/JA076i010p02213

Carveth, C., Clarke, J., Chaufray, J., & Bertaux, J. (2012, October). Analysis Of HST Spatial Profiles Of Oxygen Airglow From Mars. In *Aas/division for planetary sciences meeting abstracts #44* (Vol. 44, p. 214.03).

Chaufray, J. Y., Deighan, J., Chaffin, M. S., Schneider, N. M., McClintock, W. E., Stewart, A. I. F., ... Jakosky, B. M. (2015). Study of the Martian cold oxygen corona from the O I 130.4 nm by IUVS/MAVEN. *Geophysical Research Letters*, *42*(21), 9031-9039. Retrieved from https://agupubs.onlinelibrary.wiley.com/doi/abs/10.1002/2015GL065341 doi: https://doi.org/10.1002/2015GL065341

Chaufray, J. Y., Leblanc, F., Quémerais, E., & Bertaux, J. L. (2009). Martian oxygen density at the exobase deduced from O I 130.4-nm observations by Spectroscopy for the Investigation of the Characteristics of the Atmosphere of Mars on Mars Express. *Journal of Geophysical Research: Planets*, *114*(E2). Retrieved from https://agupubs.onlinelibrary.wiley.com/doi/abs/10.1029/2008JE003130 doi: https://doi.org/10.1029/2008JE003130

Chaufray, J. Y., Modolo, R., Leblanc, F., Chanteur, G., Johnson, R. E., & Luhmann, J. G. (2007). Mars solar wind interaction: Formation of the martian corona and atmospheric loss to space. *Journal of Geophysical Research: Planets*, *112*(E9). Retrieved from https://agupubs.onlinelibrary.wiley.com/doi/abs/10.1029/2007JE002915 doi: https://doi.org/10.1029/2007JE002915

Chirakkil, K., Deighan, J., Lillis, R., Elliott, R., Chaffin, M., Jain, S., ... AlMazmi, H. (2022, June). More than Before: Increase in Estimated Oxygen Photochemical Escape Rates from EMM Data and Updated Modeling. In *Seventh international workshop on the mars atmosphere: Modelling and observations* (p. 3554).

Cravens, T. E., Rahmati, A., Fox, J. L., Lillis, R., Bougher, S., Luhmann, J., ... Jakosky, B. (2017). Hot oxygen escape from Mars: Simple scaling with solar EUV irradiance. *Journal of Geophysical Research: Space Physics*, *122*(1), 1102-1116. Retrieved from https://agupubs.onlinelibrary.wiley.com/doi/abs/10.1002/2016JA023461 doi: https://doi.org/10.1002/2016JA023461

Deighan, J., Chaffin, M. S., Chaufray, J.-Y., Stewart, A. I. F., Schneider, N. M., Jain, S. K., ... Jakosky, B. M. (2015). MAVEN IUVS observation of the hot oxygen corona at Mars. *Geophysical Research Letters*, *42*(21), 9009-9014. Retrieved from https://agupubs.onlinelibrary.wiley.com/doi/abs/10.1002/2015GL065487 doi: https://doi.org/10.1002/2015GL065487

Eparvier, F. G., Chamberlin, P. C., Woods, T. N., & Thiemann, E. M. B. (2015, December). The Solar Extreme Ultraviolet Monitor for MAVEN. *Space Science Reviews*, *195*(1-4), 293-301. doi: 10.1007/s11214-015-0195-2

Feldman, P. D., Steffl, A. J., Parker, J. W., A'Hearn, M. F., Bertaux, J.-L., Alan Stern, S., ... Feaga, L. M. (2011). Rosetta-Alice observations of exospheric hydrogen and oxygen on Mars. *Icarus*, *214*(2), 394-399. Retrieved from https://www.sciencedirect.com/science/article/pii/S0019103511002223 doi: https://doi.org/10.1016/j.icarus.2011.06.013

Fox, J. L., & Hać, A. B. (2009). Photochemical escape of oxygen from Mars: A comparison of the exobase approximation to a Monte Carlo method. *Icarus*, *204*(2), 527-544. Retrieved from https://www.sciencedirect.com/science/article/pii/S0019103509002917 doi: https://doi.org/10.1016/j.icarus.2009.07.005

Fox, J. L., & Hać, A. B. (2014). The escape of O from Mars: Sensitivity to the elastic cross

sections. *Icarus*, *228*, 375-385. Retrieved from https://www.sciencedirect.com/science/article/pii/S0019103513004338 doi: https://doi.org/10.1016/j.icarus.2013.10.014

Fox, J. L., & Hać, A. B. (2018). Escape of O(3P), O(1D), and O(1S) from the Martian atmosphere. *Icarus*, *300*, 411-439. Retrieved from https://www.sciencedirect.com/science/article/pii/S0019103517302026 doi: https://doi.org/10.1016/j.icarus.2017.08.041

Gröller, H., Lichtenegger, H., Lammer, H., & Shematovich, V. (2014). Hot oxygen and carbon escape from the martian atmosphere. *Planetary and Space Science*, *98*, 93-105. Retrieved from https://www.sciencedirect.com/science/article/pii/S0032063314000117 (Planetary evolution and life) doi: https://doi.org/10.1016/j.pss.2014.01.007

Holsclaw, G. M., Deighan, J., Almatroushi, H., Chaffin, M., Correira, J., Evans, J. S., ... Tyagi, K. (2021, December). The Emirates Mars Ultraviolet Spectrometer (EMUS) for the EMM Mission. *Space Science Reviews*, *217*(8), 79. doi: 10.1007/s11214-021-00854-3

Jain, S. K., Stewart, A. I. F., Schneider, N. M., Deighan, J., Stiepen, A., Evans, J. S., ... Jakosky, B. M. (2015). The structure and variability of Mars upper atmosphere as seen in MAVEN/IUVS dayglow observations. *Geophysical Research Letters*, *42*(21), 9023-9030. Retrieved from https://agupubs.onlinelibrary.wiley.com/doi/abs/10.1002/2015GL065419 doi: https://doi.org/10.1002/2015GL065419

Javaraiah, J. (2011). Quasi 9 and 30–40 days periodicities in the solar differential rotation. *Advances in Space Research*, *48*(6), 1032-1040. Retrieved from https://www.sciencedirect.com/science/article/pii/S0273117711003164 doi: https://doi.org/10.1016/j.asr.2011.05.004

Leblanc, F., Modolo, R., Curry, S., Luhmann, J., Lillis, R., Chaufray, J. Y., ... Jakosky, B. (2015). Mars heavy ion precipitating flux as measured by Mars Atmosphere and Volatile EvolutioN. *Geophysical Research Letters*, *42*(21), 9135-9141. Retrieved from https://agupubs.onlinelibrary.wiley.com/doi/abs/10.1002/2015GL066170 doi: https://doi.org/10.1002/2015GL066170

Lee, Y., Combi, M. R., Tenishev, V., Bougher, S. W., Deighan, J., Schneider, N. M., ... Jakosky, B. M. (2015). A comparison of 3-D model predictions of Mars' oxygen corona with early MAVEN IUVS observations. *Geophysical Research Letters*, *42*(21), 9015-9022. Retrieved from https://agupubs.onlinelibrary.wiley.com/doi/abs/10.1002/2015GL065291 doi: https://doi.org/10.1002/2015GL065291

Lee, Y., Combi, M. R., Tenishev, V., Bougher, S. W., & Lillis, R. J. (2015). Hot oxygen corona at Mars and the photochemical escape of oxygen: Improved description of the thermosphere, ionosphere, and exosphere. *Journal of Geophysical Research: Planets*, *120*(11), 1880-1892. Retrieved from https://agupubs.onlinelibrary.wiley.com/doi/abs/10.1002/2015JE004890 doi: https://doi.org/10.1002/2015JE004890

Lillis, R. J., Deighan, J., Fox, J. L., Bougher, S. W., Lee, Y., Combi, M. R., ... Chaufray, J.-Y. (2017). Photochemical escape of oxygen from Mars: First results from MAVEN in situ data. *Journal of Geophysical Research: Space Physics*, *122*(3), 3815-3836. Retrieved from https://agupubs.onlinelibrary.wiley.com/doi/abs/10.1002/2016JA023525 doi: https://doi.org/10.1002/2016JA023525

McElroy, M. B. (1972). Mars: An Evolving Atmosphere. *Science*, *175*(4020), 443-445. Retrieved from https://www.science.org/doi/abs/10.1126/science.175.4020.443 doi: 10.1126/science.175.4020.443

McElroy, M. B., & Donahue, T. M. (1972). Stability of the Martian Atmosphere. *Science*, *177*(4053), 986-988. Retrieved from https://www.science.org/doi/abs/10.1126/science.177.4053.986 doi: 10.1126/science.177.4053.986

Montmessin, F., Korablev, O., Lefèvre, F., Bertaux, J.-L., Fedorova, A., Trokhimovskiy, A., ... Chapron, N. (2017). SPICAM on Mars Express: A 10 year in-depth survey of the Martian atmosphere. *Icarus*, *297*, 195-216. Retrieved from https://www.sciencedirect.com/science/article/pii/S0019103516308272 doi: https://

doi.org/10.1016/j.icarus.2017.06.022

Nier, A. O., & McElroy, M. B. (1977). Composition and structure of Mars' Upper atmosphere: Results from the neutral mass spectrometers on Viking 1 and 2. *Journal of Geophysical Research (1896-1977)*, *82*(28), 4341-4349. Retrieved from https://agupubs.onlinelibrary.wiley.com/doi/abs/10.1029/JS082i028p04341 doi: https://doi.org/10.1029/JS082i028p04341

Rahmati, A., Larson, D. E., Cravens, T. E., Lillis, R. J., Dunn, P. A., Halekas, J. S., ... Jakosky, B. M. (2015). MAVEN insights into oxygen pickup ions at Mars. *Geophysical Research Letters*, *42*(21), 8870-8876. Retrieved from https://agupubs.onlinelibrary.wiley.com/doi/abs/10.1002/2015GL065262 doi: https://doi.org/10.1002/2015GL065262

Rahmati, A., Larson, D. E., Cravens, T. E., Lillis, R. J., Halekas, J. S., McFadden, J. P., ... Jakosky, B. M. (2017). MAVEN measured oxygen and hydrogen pickup ions: Probing the Martian exosphere and neutral escape. *Journal of Geophysical Research: Space Physics*, *122*(3), 3689-3706. Retrieved from https://agupubs.onlinelibrary.wiley.com/doi/abs/10.1002/2016JA023371 doi: https://doi.org/10.1002/2016JA023371

Rahmati, A., Larson, D. E., Cravens, T. E., Lillis, R. J., Halekas, J. S., McFadden, J. P., ... Jakosky, B. M. (2018). Seasonal Variability of Neutral Escape from Mars as Derived From MAVEN Pickup Ion Observations. *Journal of Geophysical Research: Planets*, *123*(5), 1192-1202. Retrieved from https://agupubs.onlinelibrary.wiley.com/doi/abs/10.1029/2018JE005560 doi: https://doi.org/10.1029/2018JE005560

Strickland, D. J., Stewart, A. I., Barth, C. A., Hord, C. W., & Lane, A. L. (1973). Mariner 9 Ultraviolet Spectrometer Experiment: Mars atomic oxygen 1304-A emission. *Journal of Geophysical Research (1896-1977)*, *78*(22), 4547-4559. Retrieved from https://agupubs.onlinelibrary.wiley.com/doi/abs/10.1029/JA078i022p04547 doi: https://doi.org/10.1029/JA078i022p04547

Strickland, D. J., Thomas, G. E., & Sparks, P. R. (1972). Mariner 6 and 7 Ultraviolet Spectrometer Experiment: Analysis of the O I 1304- and 1356-A emissions. *Journal of Geophysical Research (1896-1977)*, *77*(22), 4052-4068. Retrieved from https://agupubs.onlinelibrary.wiley.com/doi/abs/10.1029/JA077i022p04052 doi: https://doi.org/10.1029/JA077i022p04052

Thiemann, E. M. B., Chamberlin, P. C., Eparvier, F. G., Templeman, B., Woods, T. N., Bougher, S. W., & Jakosky, B. M. (2017). The MAVEN EUVM model of solar spectral irradiance variability at Mars: Algorithms and results. *Journal of Geophysical Research: Space Physics*, *122*(3), 2748-2767. Retrieved from https://agupubs.onlinelibrary.wiley.com/doi/abs/10.1002/2016JA023512 doi: https://doi.org/10.1002/2016JA023512

Yagi, M., Leblanc, F., Chaufray, J., Gonzalez-Galindo, F., Hess, S., & Modolo, R. (2012). Mars exospheric thermal and non-thermal components: Seasonal and local variations. *Icarus*, *221*(2), 682-693. Retrieved from https://www.sciencedirect.com/science/article/pii/S0019103512002989 doi: https://doi.org/10.1016/j.icarus.2012.07.022